Research article

Qunhuo Liu, Ying Tian*, Wenhua Tang, Xufeng Jing, Junjie Zhang and Shiqing Xu*

Comprehensive studies of the Ag^+ effect on borosilicate glass ceramics containing Ag nanoparticles and Er-doped hexagonal $NaYF_4$ nanocrystals: morphology, structure, and 2.7 μm emission

https://doi.org/10.1515/nanoph-2018-0024
Received February 20, 2018; revised April 1, 2018; accepted April 9, 2018

Abstract: In this work, we have performed a comprehensive investigation of the Ag^+ concentration effect on the morphological, thermal, structural, and mid-infrared emission properties of novel oxyfluoride borosilicate glasses and glass ceramics containing both Ag nanoparticles and erbium-doped hexagonal $NaYF_4$ nanocrystals. The effect of Ag^+ ions on the glass forming and crystallization processes was discussed in detail by glass structural analysis. It was found that the Ag^+ concentration can affect the distribution of Na^+ ion and bridge oxygen in boron-rich and silicon-rich phases, which induced the transformation between BO_3 triangles and BO_4 tetrahedra during crystallization process. In addition, there was a turning point when the doped Ag^+ ion concentration reached its solubility in the borosilicate glass. Furthermore, the enhancement of the 2.7 μm emission and the reduction of the lifetime of the $^4I_{13/2}$ level were observed both in glasses and in glass ceramics, and its origin was revealed by qualitative and quantitative analyses of the Er^{3+}-Ag nanoparticles (localized electric field enhancement) and Er^{3+}-Er^{3+} (nonradiative resonance energy transfer) interactions within glasses and glass ceramics. Moreover, the high lifetime of the $^4I_{11/2}$ level (2.12 ms) and the peak emission cross section in 2.7 μm (6.8×10^{-21} cm^2) suggested that the prepared glass ceramics have promising mid-infrared laser applications.

Keywords: Ag nanoparticles; glass and glass ceramic; glass structure; mid-infrared emission.

***Corresponding authors: Ying Tian and Shiqing Xu,** College of Materials Science and Engineering, China Jiliang University, Hangzhou 310018, P.R. China, e-mail: tianyingcjlu@163.com (Y. Tian); sxucjlu@163.com (S. Xu)
Qunhuo Liu, Wenhua Tang and Junjie Zhang: College of Materials Science and Engineering, China Jiliang University, Hangzhou 310018, P.R. China
Xufeng Jing: Institute of Optoelectronic Technology, China Jiliang University, Hangzhou 310018, P.R. China

1 Introduction

A novel type of glasses containing both rare earth (RE) ions and Ag ions has emerged in recent years but has already attracted considerable attention [1–3]. The reason for such interest lies in the efficient enhancement of the fluorescent properties in RE-doped glasses when introducing appropriate Ag ions. The Ag exists in glass mainly in the forms of isolated Ag^+ ions (or Ag atoms), molecular-like Ag nanocluster, or Ag nanoparticles (Ag NPs) with surface plasmonic resonance (SPR) absorption bands [2]. The SPR effect plays an intriguing role in material design, photonics, and other applications [4–7]. In particular, the fluorescent enhancement by Ag NPs is due to the enhanced electromagnetic field surrounding the Ag NPs, tuning the radiative decay properties of neighboring RE ions [8, 9]. So far, many researchers have been conducted to study the formation mechanism of Ag NPs in glass [2, 10] and relative factors, including Ag doping concentration [11], glass host composition [12], and the afterward thermal treatment [13, 14]. Besides, the spectroscopic properties of glasses containing both RE ions and Ag NPs in the visible and near-infrared ranges were also deeply investigated [15, 16]. The spectroscopic properties of such a new hybrid material in the mid-infrared (MIR) range, however, have received far less attention and are consequently less clear.

The MIR emission is of particular importance because most molecules display high absorption cross section in this region and therefore have promising applications in chemical and biomolecular sensing and food quality control [17, 18]. Advanced applications demand an efficient MIR emission, and there are ongoing efforts to design highly efficient MIR emission materials. RE-doped oxyfluoride glass ceramics (GCs) are one of the most efficient MIR materials and have long fascinated many researchers [19]. The attraction of oxyfluoride GCs is that they can simultaneously meet two critical requirements for MIR laser materials: low phonon energy and excellent macroscopic properties. On one hand, fluoride nanocrystals (NCs) contained in the glass matrix provide low phonon energy environment for RE dopant, which can weaken the

multiphonon-assisted nonradiative relaxation effect and enhance the fluorescent efficiency of RE ions [20]. On the other hand, oxide glass matrices exhibit excellent macroscopic properties such as thermal stability, mechanical properties, and chemical durability that are important for practical applications such as fiber amplifiers [21, 22].

Some researches have proved that the introduction of Ag NPs can enhance the MIR emission of RE-doped glass [23–25]. However, to the best of our knowledge, there was no report on the effect of Ag NPs on the structure and MIR emission of RE-doped GCs, which is more complex and promising because of the complicated structure and better performance of GCs. Among oxyfluoride GCs, oxyfluoride borosilicate GCs have the advantages of excellent stability of silicate glass and higher Ag ion solubility of borate glass [26], offering a good chance to explore Ag-doped oxyfluoride GCs as a new MIR material. In this context, we set out to carry out a combined experimental and theoretical study on the structure and MIR emission of oxyfluoride borosilicate glasses and GCs containing both Er-doped fluoride NCs and Ag NPs.

In this work, novel oxyfluoride borosilicate GCs containing Er-doped hexagonal $NaYF_4$ (β-$NaYF_4$) NCs and Ag NPs were successfully prepared. The morphological characteristics and absorption spectra are studied to confirm the existence of β-$NaYF_4$ NCs and Ag NPs in glass. The thermal properties were investigated to guide the heat treatment condition and assess the change of structural tightness. Together with vibration spectra, the change of glass structure was deeply revealed. Finally, the MIR emission properties of glasses and GCs with different Ag^+ concentration doping were analyzed, and the origin of fluorescence change was discussed in detail.

2 Experimental procedures

2.1 Samples preparation

The microstructure and luminescent behaviors of GCs are largely affected by Ag^+ doping concentration, especially when doping concentration reached its solubility in glass; therefore, a series of GCs with different Ag^+ concentration were prepared. More importantly, for the deep investigation of structural evolution and luminescent mechanism of GCs, glass samples with the same concentration were necessary to be synthesized and analyzed for comparison. Glasses with the molar composition of $58SiO_2$-$14.5H_3BO_3$-$13.5Na_2CO_3$-6NaF-$5.5YF_3$-$0.5ErF_3$-$xAgNO_3$ ($x = 0$, 0.1, 0.3, 0.5, and 1, corresponding to G0, G0.1, G0.3, G0.5, and G1) were melted from analytical grade powders (all reagents were bought from Aladdin Industrial Corporation, Shanghai, China). The raw materials with required proportion were mixed homogeneously and put into a covered corundum crucible in order to prevent the vaporization of fluoride. Then the crucibles were placed in an elevator furnace (YFG200*250/170-YC, Shanghai Y-feng Electrical Furnance Ltd, Shanghai, China) at 1450°C, where it remained for 30 min. After melting, the glasses were quenched on preheated stainless steel plated before being annealed at 500°C for 30 min to release inner stress. Each glass was cut into two pieces properly, and these glasses were divided into two batches.

Transparent GCs were obtained by the traditional partial devitrification-controlled crystallization of starting glasses [22]. One batch of the above glasses was put into a muffle furnace at 600°C for 12 h to acquire GCs, which are correspondingly denoted as GC0, GC0.1, GC0.3 GC0.5, and GC1, respectively. Based on glass characteristic temperature analyzed below, the thermal treatment temperature was chosen as the moderate value of 600°C in order to ensure that the sample remains transparent and the crystal phase stable. Finally, the glasses and GC samples were cut and polished into the glass samples with thickness of 1 mm for thermal, structural, and spectroscopic properties measurements.

2.2 Characterization

The densities of glass samples were measured according to the Archimedes principle using distilled water as the immersion liquid. The differential scanning calorimetry (DSC) curves for powder glass samples were measured by a differential thermal analysis (DTA 404PC, NETZSCH, Free State of Bavaria, Germany) at the heating rate of 10 K/min. To know the difference between glasses and GCs, X-ray diffraction (XRD) analysis of the samples was performed with a X-ray diffractometer(D2 PHASER, Bruker, Karlsruher, Germany) using Cu-$K_{\alpha 1}$ radiation. The micrographs of GC were measured by a transmission electron microscope (TEM, Tecnai G2 F20, FEI, Hillsboro, OR, USA). Fourier transform infrared (FTIR) spectra were measured by FTIR spectrometer (Nicolet iS50, Thermo Fisher Scientific Inc., MA, USA) in the range of 400–1500 cm^{-1}. Absorption spectra were measured by a UV-VIS-NIR spectrophotometer (UV3600, Shimadzu Corporation, Kyoto, Japan) with a resolution of 1 nm, and diffuse reflectance spectra were measured in the same instrument using $BaSiO_4$ (99%, 1 μm) as references. Upconversion visible spectrum was examined by a fluorescence spectrometer-Fluorolog (Fl-3-211, Jobin Yvon, Paris, France), and a 980 nm laser diode was used as the excitation source. MIR emission spectra were measured

by MIR emission spectrometer (FLS980, Edinburgh Instruments Ltd, Livingston, UK). and detected with a liquid-nitrogen-cooled PbS detector upon excitation by a 980 nm laser diode. All the measures were taken at room temperature, and other conditions were kept as similar as possible.

3 Results and discussion

3.1 Morphological characteristics

The XRD for glasses and GCs were measured by powders of glass samples after polishing. The amorphous nature of the glasses was confirmed by the absence of peaks in Figure 1A. Crystallization of the β-$NaYF_4$ phase was observed for all GC samples, as the diffraction peaks of the XRD curve in Figure 1B were well matched with the standard pattern of β-$NaYF_4$ (PDF#16-0334). However, the Ag NPs are undetectable in both glasses and GCs from XRD analysis, supposedly because of the small size of Ag NPs. Interestingly, surface crystallization phenomenon was observed in GC1 sample, and the surface crystallized layer was also measured by XRD using bulk GC1 sample, as shown in Figure 1C. The result indicates that the crystallization phase was formed in the surface crystallized layer, corresponding to SiO_2 (PDF#42-1401) and Ag (PDF#65-2871) crystals. The crystallization of glass surface is brought about by two reasons. On one hand, the aggregated Ag NPs can play a role as nucleating agent for the crystallization of stable oxide components in glass when the doped Ag^+ ion concentration is higher than its solubility in the borosilicate glass. On the

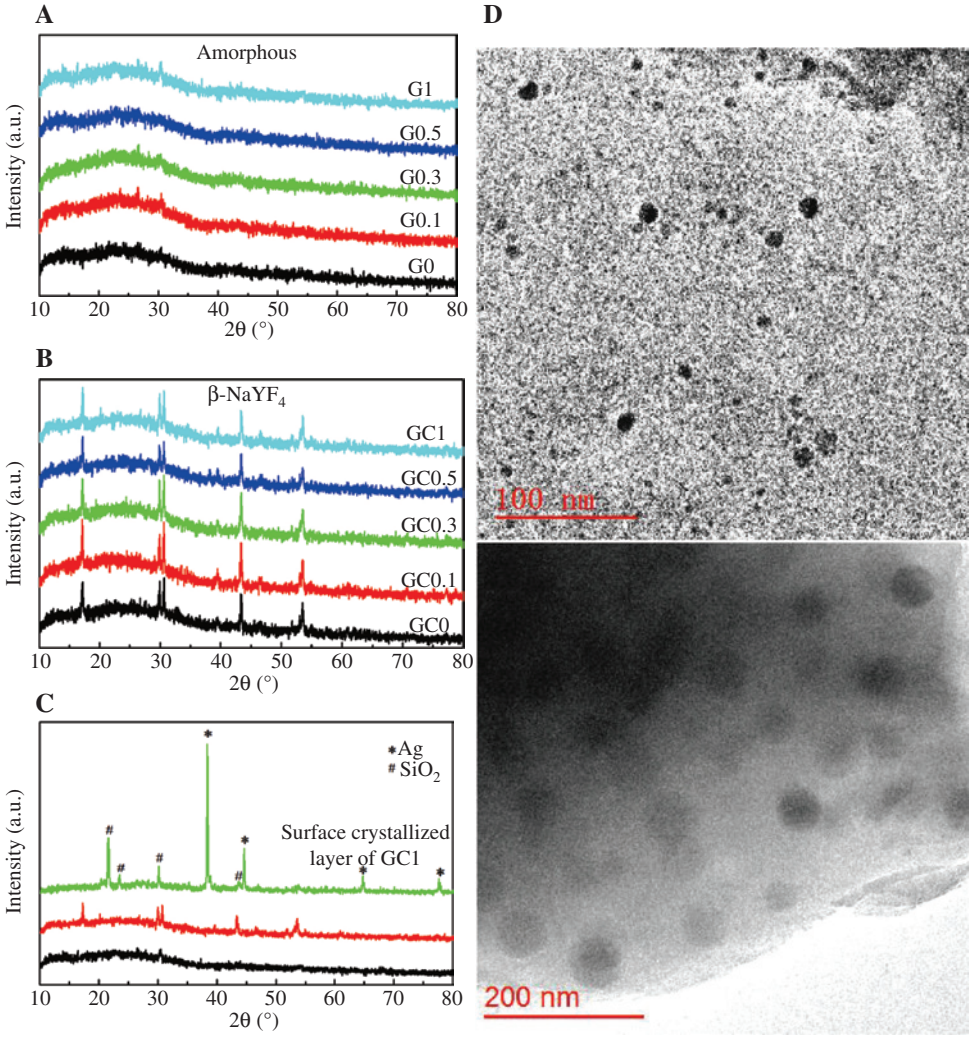

Figure 1: Morphological characteristics of glasses and GCs.
XRD patterns of glasses (A) and GCs (B); (C) comparison of the XRD patterns for the G1 sample, GC1 sample, and surface crystallized layer of the GC1 sample; TEM micrographs of Ag NPs (D) and β-$NaYF_4$ NCs (E) distributed in glass.

other hand, the resistance of the rearrangement and migration of atoms is relatively small in glass surface, which has more breaking bonds than glass interior. Figure 1D and E show TEM micrographs of Ag NPs and β-$NaYF_4$ NCs distributed in glass, captured from powders of the G0.1 and GC0.5 samples, respectively. The Ag NPs of varying diameters mainly from 6 to 13 nm are inhomogeneously distributed in glass, while β-$NaYF_4$ NCs with diameters of roughly 45–65 nm are homogeneously distributed in glass.

3.2 Thermal and structural analysis

The DSC thermograms of different concentrations of Ag dopants in glasses are shown in Figure 2A. Two exothermal peaks can be observed for each glass sample. The first weak exothermal peak near 625°C is caused by the crystallization of fluoride components in the glass, while the second broad exothermal peak can be attributed to the crystallization of borosilicate oxides in the glass matrix. The variation of glass transition temperature T_g, which is sensitive to any change in the coordination number of the network forming atoms and the formation of nonbridging oxygen (NBO) bonds, was able to indicate the structural changes in the glass network. It is noticeable that the T_g of glass samples firstly decreases from G0 to G0.5 and then increases from G0.5 to G1. Thus, the number of NBO bonds in glass structure increases firstly and then reduces at different Ag doping concentration. $\Delta T = T_{x2} - T_g$ (T_{x2} is the onset crystallization temperature for the second exothermal peak) is generally considered as a

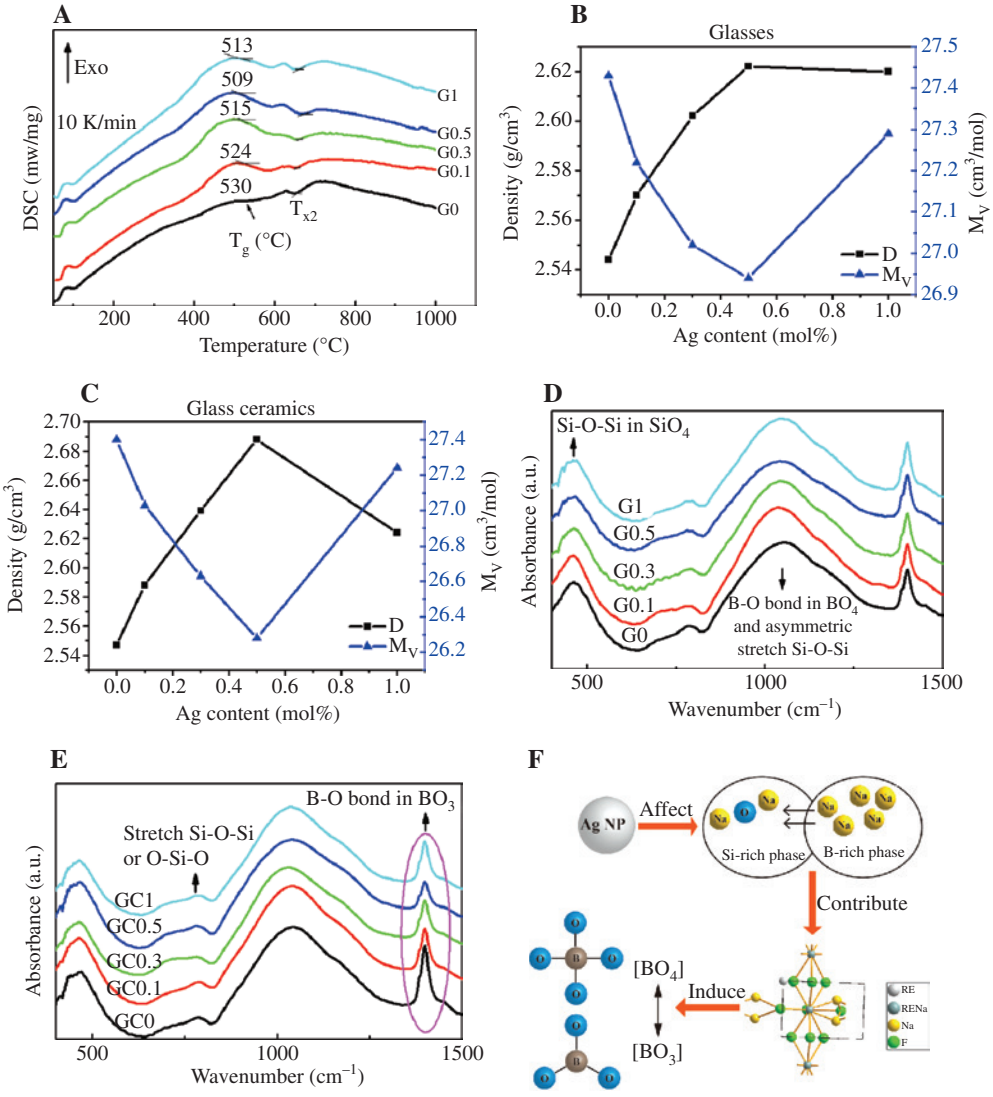

Figure 2: Effect of Ag^+ on the thermal properties and structure variation of glasses and GCs.
(A) DSC curves of the borosilicate glasses; densities and molar volume of glasses (B) and GCs (C); Fourier transform infrared absorption spectra of glasses (D) and GCs (E); (F) schematic structure variation of glass due to the introduction of Ag NPs.

useful criteria for evaluating the thermal stability of glass and the accessibility of fiber drawing. Here, one can find that the ΔT of glass samples firstly increases (126°C, 133°C, 145°C, 165°C, and 148°C, corresponding to G0, G0.1, G0.3, and G0.5, respectively) and subsequently decreases from G0.5 to G1. The result indicates that appropriate addition of Ag in the investigated glass is favorable for enhancing the thermal stability of glass.

The density measurement gives a rough macroscopic overview of the structural packing. The measured density and calculated molar volume of glasses and GCs have been presented in Figure 2B and C, respectively. The density was found to be proportional to the increase of Ag content, which is most likely related to the addition of $AgNO_3$ with high molar mass. However, the density later decreases with the further improvement of Ag^+ ion concentration, suggesting that a structure change occurs in glass. The glass structure tends to be in order after the crystallization process of β-$NaYF_4$, leading to the increment of density in all GCs compared with corresponding precursor glasses.

To identify the presence of different structural groups and possible changes in their rearrangement with the glass composition, normalized FTIR absorption spectra of glasses and GCs are shown in Figure 2D and E, respectively. The main characteristic IR bands for glasses and GCs are as follows [27–30]:

(i) The bands at around 470 cm^{-1} are attributed to the vibration of Si-O-Si bonds containing SiO_4 tetrahedra.
(ii) The weak bands near 785 cm^{-1} are related to the stretching vibration of Si-O-Si or O-Si-O.
(iii) The broad bands in the region 800–1300 cm^{-1} are due to the deformation and asymmetric stretching vibrations of the B-O bond in the BO_4 tetrahedra and asymmetric stretching vibrations of the Si-O-Si bonds in complex anions.
(iv) The peaks close to 1400 cm^{-1} are associated with the stretching vibration of the B-O bond in the composition of the BO_3 triangles.

It can be seen that the position of the broad band in the region 800–1300 cm^{-1} is slightly shifted, which may be caused by the change of NBO in glasses and GCs. Furthermore, the intensity of peaks near 1400 cm^{-1} has no obvious change in glass samples while it decreases previously and increases later in GCs with an increase in Ag-doped concentration. The change in intensity of this peak is indicative of the fact that the interconvert of BO_3 triangles and BO_4 tetrahedra occurred in the glass structure.

To deeply reveal the change in the glass structure, the distributed tendency of Na^+ and Ag^+ in such phase-separated glasses is first determined. The Na^+ ions in the glasses can either attach with silicon as Si^--Na^+ resulting in the formation of NBO or with boron by forming an alkali borate phase. The association of the Na^+ ions with boron or silicon is governed by the R and K ratios (where $R = [Na_2O]/[B_2O_3]$ and $K = [Na_2O]/[SiO_2]$). The sodium ions associate with boron till $R < 0.5$ and thereafter link with silicon. Also, it has been found that in sodium borosilicate glasses, if $K > 0.5$, then the sodium ions link only with boron [28]. Therefore, a certain amount of Na^+ ions associate with boron, and residual Na^+ ions link with silicon in the investigated glasses, where $K < 0.5$ and $R > 0.5$. Besides, it is reported that most of the Ag^+ ions are preferentially dispersed in the B_2O_3-rich glassy phase compared with the SiO_2-rich glassy phase [26]. Therefore, a simplified influence mechanism for glass structure variation is shown in Figure 2F and is summarized as follows:

In the glass forming process (melting-quenching stage), the Ag^+ ions can displace Na^+ ions in the boron-rich phase, resulting in more displaced Na^+ ions entering into the Si-O network in order to keep the charge balanced. Thus, the number of BO_3 triangles has little change in the investigated glasses. More Na^+ ions in silicon-rich phase can break Si-O bonds resulting in more loose glass structure and decreased T_g. However, for glass doped with higher Ag^+ concentration (G1 sample), the network of glass becomes B_2O_3-deficient so that the excessive Ag^+ ions participate in the formation of the Si-O network, leading to decreased Na^+ ions in Si-O network and the rebound of T_g.

In the crystallization process (heat treatment stage), Na^+ ions in the Si-O network take part in the formation of β-$NaYF_4$ NCs and accompany with the free oxygen. The emerging free oxygen would affect the glass structure because the melted B_2O_3 composition has a layered structure while the melted SiO_2 composition possesses a framework structure. Combined with the free oxygen, BO_3 triangles in glass are translated to BO_4 tetrahedra, which converts the layered structure of boron to the framework structure and increases the connectivity of the whole glass network, creating the condition for B_2O_3 and SiO_2 to form a uniform glass network. Accordingly, the number of BO_3 triangles is decreased and the number of BO_4 tetrahedra is increased in GC samples (from GC0 to GC0.5) as reflected by the FTIR spectra. However, for the GC1 sample, Ag and SiO_2 crystals precipitate in heat treatment process due to excessive Ag^+ ions in Si-O network. The crystallization of SiO_2 phases in glass surface would prompt Na^+ ions into the boron-rich phase, resulting in decreased BO_4 tetrahedra and increased BO_3 triangles in the glass network.

3.3 Absorption spectra and MIR emission properties

The absorption spectra of glasses and GCs at room temperature ranging from 500 to 1750 nm are presented in Figure 3A and B, respectively. Similar to other Er^{3+}-doped glass system [31], there are five absorption peaks centered at around 521, 530, 650, 796, 976, and 1530 nm, corresponding to the transitions starting from the Er^{3+}:$^4I_{15/2}$ ground state to its excited state levels $^2H_{11/2}$, $^4S_{3/2}$, $^4F_{9/2}$, $^4I_{9/2}$, $^4I_{11/2}$, and $^4I_{13/2}$, respectively. The strong absorption peaks centered at 976 nm indicate that the Er^{3+} ion doped glasses and GCs can be pumped by commercial 980 nm laser diodes. However, the absorption spectra of some samples ranging from 300 to 500 nm were over-ranged. In this case, the diffuse reflectance spectra of the powders of samples were measured to reveal the absorptive characteristics of samples in the 300–500 nm region, as shown in Figure 3C and D. Here, one can clearly find the characteristic SPR bands at around 410 nm in Ag^+ ion doped glasses and GCs. The plasmon resonance wavelength depends upon the size of Ag NPs, and it increases with the diameter of Ag NPs [32–34]. Obviously, it can be seen that the plasmon resonance wavelength shows a red shift when doped Ag^+ ion concentration increases, indicating the increased size of aggregated Ag NPs [14, 32]. The average particle size of Ag NP in G0.1 sample can be estimated to be around 10 nm by the simulation of SPR peak wavelengths [32]. This is in agreement with the TEM micrograph in Figure 1D. The intense SPR bands in the diffuse reflectance spectra suggest that Ag NPs are abundant in glass samples. In addition, the intensity of SPR bands decreases from G0.1 to G1. This is because the barrier to form bigger Ag NPs is higher so that the number of Ag NPs in glass is smaller after the short-annealing process. Whereafter, the long thermal treatment process provides sufficient energy for the formation of large Ag NPs, resulting in more intense SPR bands of diffuse reflectance spectra in Ag^+-doped GCs. However, the intensity of the SPR band of GC1 sample shows a rebound, which is attributed to its surface crystallization behavior as discussed in the above section. Furthermore, the spectral broadening of SPR band in glass can be attributed to plasmon hybridization, which can be viewed as bonding and antibonding combinations of individual nanosphere plasmons [14, 35].

Figure 4A and B present the fluorescence spectra of Er^{3+}-doped glasses and GCs in the spectral region of 2500–3000 nm pumped at 980 nm as a function of Ag^+ ion doping concentration, respectively. It is found both in glasses and GCs that the intensity of 2.7 μm emission increases with the increment of Ag^+ content, and the fluorescence enhancement was more obvious in glasses than

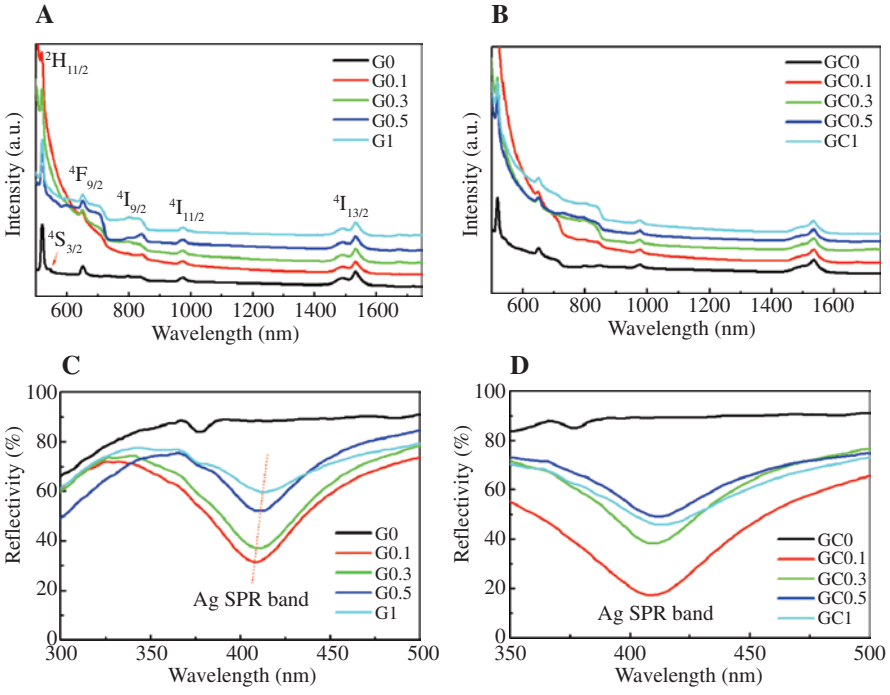

Figure 3: Absorption features of Er^{3+} ions and Ag NPs in glasses and GCs.
Absorption spectra ranging from 500 to 1750 nm of glasses (A) and GCs (B); diffuse reflectance spectra ranging from 300 to 500 nm in glasses (C) and GCs (D).

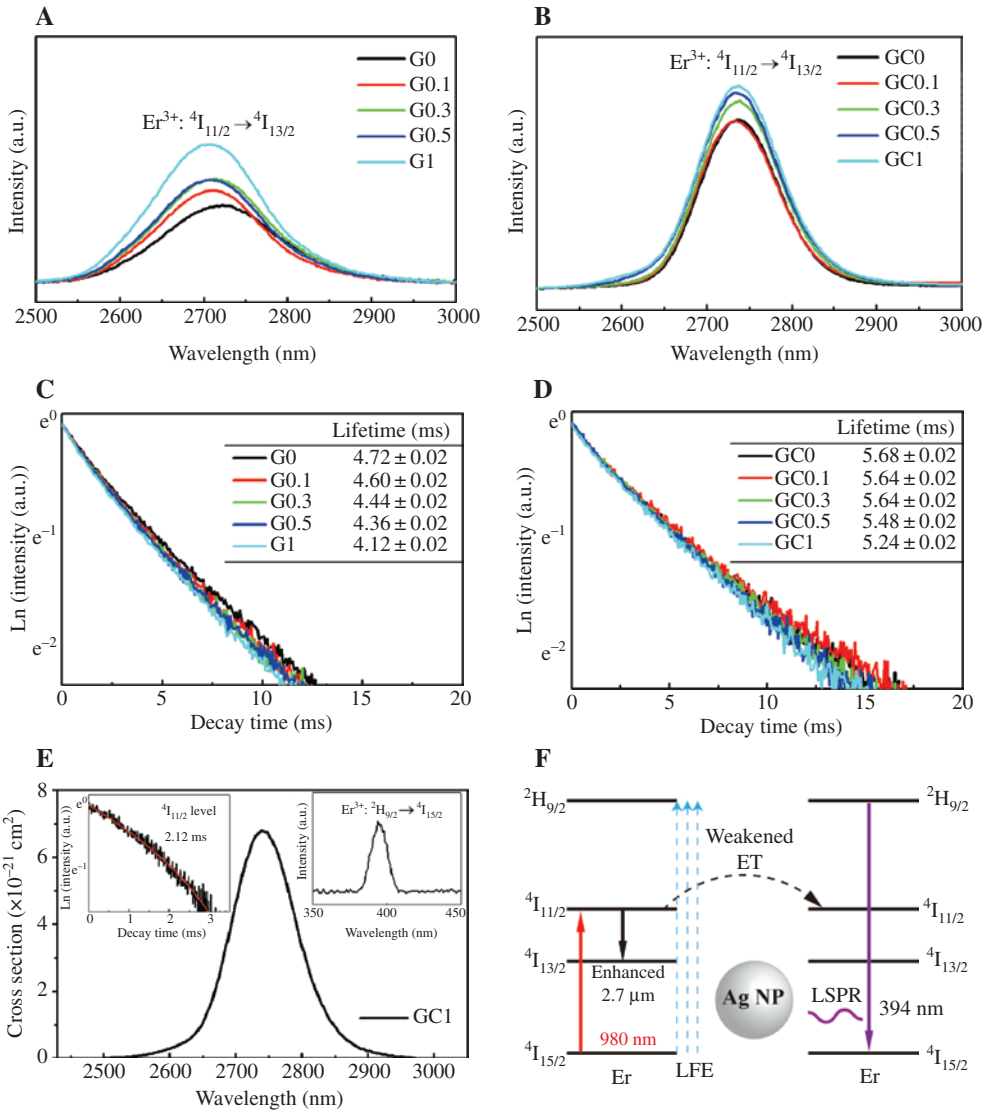

Figure 4: Mid-infrared emission properties of glass and GCs.
The 2.7 μm emissions of glasses (A) and GCs (B); decay curves and lifetime of $^4I_{13/2}$ level in glasses (C) and GCs (D); (E) calculated emission cross section in 2.7 μm, lifetime of the $^4I_{11/2}$ level (inset at the left), and upconversion emission spectrum (inset at the right) of the GC1 sample; (F) schematic simplified energy level diagram of Er^{3+} ions and the fluorescence enhancement mechanism.

in GCs. Figure 4C shows that the decay lifetime of the $^4I_{13/2}$ level in glasses reduces from 4.72 to 4.12 ms with increasing Ag^+ ions content. A similar phenomenon was observed in GCs; however, the degree of decrease is smaller, as shown in Figure 4D. The decreased lifetime of $^4I_{13/2}$ level is beneficial to the population between the upper $^4I_{11/2}$ level and the lower $^4I_{13/2}$ level of Er^{3+} ions, which can improve the 2.7 μm fluorescence intensity and laser output.

The 2.7 μm emission cross section of the GC1 sample is subsequently calculated by the Füchtbauer-Ladenburg equation [36]:

$$\sigma_{em} = \frac{\lambda^5 A_{rad}}{8\pi c n^2} \frac{I(\lambda)}{\int \lambda I(\lambda) d\lambda} \quad (1)$$

where λ is the wavelength, $I(\lambda)$ is the measured fluorescence intensity, $I(\lambda)/\int \lambda I(\lambda) d\lambda$ is the normalized line shape function of the experimental emission spectrum, A_{rad} is the radiative transition probability, and c and n are the light speed in vacuum and the index of refraction, respectively. The spontaneous transition probability A_{rad} (here the value is 26.45 s^{-1}) was obtained based on the measured absorption spectrum and the Judd-Ofelt theory [37, 38]. The calculated peak emission cross section is 6.8×10^{-21} cm^2, which is larger than that of the $LiYF_4$ crystal (5.3×10^{-21} cm^2) [39] and the ZBLAN glass fiber (5.7×10^{-21} cm^2) [40]. As shown in Figure 4E's inset at the left, the lifetime of the $^4I_{11/2}$ level in the GC1 sample is 2.12 ms (measured under 808 nm pumping), which is much larger than that in the lanthanum-tellurite

glass (0.21 ms) [41], the germanate glass (0.24 ms) [42], and the fluorotellurite glass (1.07 ms) [43]. Furthermore, based on the measured lifetime and calculated radiative lifetime, the overall fluorescence quantum efficiency (η) of the $^4I_{11/2}$ level was determined by the following relationship:

$$\eta = \frac{\tau_{fl}}{\tau_{rad}} \tag{2}$$

The calculated value of η was as high as 35.7%. The high quantum efficiency in such material is mainly because β-$NaYF_4$ NC is one of the lowest phonon energy in luminescent materials, in which the multiphonon nonradiative decay rate is much smaller. The high emission cross section and quantum efficiency suggest that the prepared GCs have good gain properties and potential MIR laser applications.

3.4 Origin of enhanced MIR emission

The dynamics of emission and energy transfer (ET) process are strongly associated with the distance between different or same doped ions, NPs and NCs in glass. The average distances for Er^{3+}-Er^{3+} and Er^{3+}-Ag^+ ion pairs are calculated using the following equation [44]:

$$R = \left(\frac{M}{N_A \rho x}\right)^{\frac{1}{3}} \tag{3}$$

where M is the mean molecular weight of borosilicate glass, N_A is the Avogadro number, ρ is the glass density, and x is the total concentration of the incorporated Er^{3+} or Ag ions. The distance between two Er^{3+} ions in β-$NaYF_4$ NCs can be estimated using the following equation [45]:

$$R \approx 2\left(\frac{3V}{4\pi x_c N}\right)^{\frac{1}{3}} \tag{4}$$

where N is the number of molecules in the unit cell, V is the cell volume, and x_c is the total concentration of doped Er^{3+} ions. In the case of β-$NaYF_4$ NCs, the number of molecules is equal to 1, and the cell volume is 108.6 $Å^3$. As the heat treatment time is as long as 12 h, it is a reasonable assumption that all NaF, YF_3, and ErF_3 are formed as NCs. The x_c in NCs is calculated in consideration of these raw materials. The calculated distances are shown in Table 1. Although the Ag^+ ions distributed in glass aggregate to form Ag NPs, the average distance of Ag^+-Er^{3+} ion pair has reference significance to the distance between Ag NPs and Er^{3+} ions as they are expected to have a similar trend.

Table 1: The average distances of Er^{3+}-Er^{3+} and Ag^+-Er^{3+} ion pairs and the energy transfer coefficients of Er^{3+}:$^4I_{11/2} \rightarrow Er^{3+}$:$^4I_{11/2}$ resonance energy transfer process.

Sample	$d_{Er\text{-}Er}$ (Å)	$d_{Ag\text{-}Er}$ (Å)	C_{DA} (10^{-41} cm^6 s^{-1})
G0	20.89	/	1.97
G0.1	20.83	19.60	1.90
G0.3	20.78	17.77	1.71
G0.5	20.40	16.48	1.64
G1	20.85	13.89	1.56
GC0	17.07	/	/

In the present glass samples, the vast majority of Ag^+ ions coalesces and exists in the form of nonluminescent Ag NPs so that the ET from Ag atoms or molecular-like Ag to Er^{3+} ions is negligible. Therefore, we discuss the interaction between Ag NPs and Er^{3+} ions here. From diffuse reflectance spectra, the localized surface plasmon resonance effect will emerge when the wavelength of light interacting with Ag NPs is in the range of 300–500 nm. At the same time, the $^2H_{9/2} \rightarrow {}^4I_{15/2}$ transition of Er^{3+} ions can radiate a 394 nm light, as shown in Figure 4E's inset at the right. Therefore, as shown schematically in Figure 4F, the localized electric field (LFE) around nearby Er^{3+} ions can be increased by the localized surface plasmon resonance effect when the Ag NPs interact with the 394 nm light. Furthermore, the Er^{3+}:$^4I_{11/2}$ level was influenced by the enhanced LFE, so the phonon mode density and the radiation rate of Er^{3+}:$^4I_{11/2} \rightarrow {}^4I_{13/2}$ were increased [46]. In this case, the 2.7 μm emission of Er^{3+} ions was improved, as has been proved in Figure 3. With increasing Ag^+ ion concentration, the size of Ag NPs increased, and the distance between Er^{3+} ions and Ag NPs decreased, suggesting the enhancement of the LFE in the proximity of Er^{3+} ions, thereby enhancing the Er^{3+} ions' MIR emission in glass samples. However, the Er^{3+} ions in β-$NaYF_4$ NCs are farther from the Ag NPs and thus are affected far less.

In addition to the interesting Er^{3+}-Ag NP interaction, the origin of the change in MIR emission can be learned from the Er^{3+}-Er^{3+} interactions within the glasses and GCs. When two active ions are placed in close proximity, they could interact by multipolar electric coupling, inducing nonradiative ET between active ions. The ET process can be quantitatively evaluated by the calculations of the absorption and emission cross sections of Er^{3+} ions using Dexter theory [47], and the Dexter expression for the ET coefficient (C_{DA}) by dipole-dipole mechanism can be expressed as follows:

$$C_{DA} = \frac{6cg_{low}^{D}}{(2\pi)^4 n^2 g_{up}^{D}} \sum_{m=0}^{\infty} e^{-(2\bar{n}+1)S_0} \frac{S_0^m}{m!} (\bar{n}+1)^m \int \sigma_{ems}^{D}(\lambda_m^+) \sigma_{abs}^{A}(\lambda) d\lambda \quad (5)$$

where D and A are the donor and accepter, respectively, (both are Er^{3+} ions in this work). g_{low}^{D} and g_{up}^{D} are the degeneracy of the lower and upper levels of the donor, respectively. $\hbar\omega_0$ is the maximum phonon energy, $\bar{n}$ is the average occupancy, m is the number of phonons participating in the ET (no phonon is necessary for resonance ET), S_0 is the Huang-Rhys factor, and $\lambda_m^+ = 1/(1/\lambda - m\hbar\omega_0)$ is the wavelength with m phonon creation. The absorption and emission cross sections can be obtained from the measured absorption spectra and McCumber formula [48], and the calculation method has been well discussed in other reports.

The C_{DA} of ET (Er^{3+}:$^4I_{11/2} \rightarrow Er^{3+}$:$^4I_{11/2}$) have been calculated for all glass samples and are present in Table 1. Generally, the ET efficiency increases with the decrease of the D-A distance due to the electric coupling effect. However, the calculated C_{DA} of ET (Er^{3+}:$^4I_{11/2} \rightarrow Er^{3+}$:$^4I_{11/2}$) decreases with the decrease of the Er^{3+}-Er^{3+} distance in glass samples, as shown in Table 1. This indicates that the Er^{3+} ions in the $^4I_{11/2}$ level incrementally radiate their energy to lower levels instead of nonradiatively transferring energy to adjacent Er^{3+} ions, which also confirms the LFE effect on MIR emission by surrounding Ag NPs, as shown in Figure 4F.

As there would be a rigid restriction on the distance between two Er^{3+} ions in β-$NaYF_4$ NCs, the calculation of such a resonance ET between two Er^{3+} ions in β-$NaYF_4$ NCs is sensitive to the calculated cross sections. However, the measured absorption spectra of GCs insufficiently support the calculation of cross sections for β-$NaYF_4$ NCs. This complicates the determination of C_{DA} in GCs. Even so, we can qualitatively know that the distance between Ag NPs and Er^{3+} ions in β-$NaYF_4$ NCs is larger than the distance between Ag NPs and Er^{3+} ions in glass because the diameter of β-$NaYF_4$ NCs are dozens of nanometers. As a result, the emission of a single Er^{3+} ion and the ET process between two Er^{3+} ions are affected less by the formation of Ag NPs in GCs, leading to a small enhancement of the MIR emission in GCs.

4 Conclusion

In conclusion, different concentrations of Ag^+ ions with Er^{3+}-doped oxyfluoride borosilicate glasses and GCs were prepared by melting-quenching method. XRD, absorption spectra, and TEM confirmed that the prepared GCs contain Ag NPs together with β-$NaYF_4$ NCs. DSC, densities, and FTIR absorption spectra of samples led us to analyze the structural change of glass, revealing the effect of Ag^+ ions on the glass forming process and crystallization process. It was found that the Ag^+ concentration can affect the distribution of Na^+ ion and bridge oxygen in boron-rich and silicon-rich phases, which induced the transformation between BO_3 triangles and BO_4 tetrahedra during crystallization process. In addition, there was a turning point when the doped Ag^+ ions concentration reached its solubility in borosilicate glass. Besides, the influence of aggregated Ag NPs on 2.7 μm emission was studied, and its origin was revealed by qualitative and quantitative analyses of the Er^{3+}-Ag NPs (LFE effect) and Er^{3+}-Er^{3+} (ET) interactions within glass and GX. Furthermore, the high lifetime of the $^4I_{11/2}$ level (2.12 ms) and the peak emission cross section in 2.7 μm (6.8×10^{-21} cm^2) of GC suggested that the prepared GCs have promising MIR laser applications. Moreover, the 2.7 μm fluorescent enhancement due to the LFE effect was more obvious in glass than in GC, which is found to be related to the size of Ag NPs and the distance between Ag NPs and Er^{3+} ions. The structure and MIR luminescence on this hybrid glass material were investigated by multiple methods, providing a deeper comprehension of the complicated glass structure and a new choice for MIR laser host materials.

Acknowledgments: The authors are thankful to the National Natural Science Foundation of China (nos. 61775205 and 51472225), the Zhejiang Provincial Natural Science Foundation of China (no. LD18F050001), and the National Natural Science Foundation of China (nos. 61405182 and 61605192).

References

[1] Kuznetsov AS, Tikhomirov VK, Shestakov MV, Moshchalkov VV. Ag nanocluster functionalized glasses for efficient photonic conversion in light sources, solar cells and flexible screen monitors. Nanoscale 2013;5:10065–75.
[2] Simo A, Polte J, Pfänder N, Vainio U, Emmerling F, Rademann K. Formation mechanism of silver nanoparticles stabilized in glassy matrices. J Am Chem Soc 2012;134:18824–33.
[3] Diez I, Ras RHA. Fluorescent silver nanoclusters. Nanoscale 2011;3:1963–70.
[4] Lan G, Liu S, Zhang X, Wang Y, Song Y. Highly sensitive and wide-dynamic-range liquid-prism surface plasmon resonance refractive index sensor based on the phase and angular interrogations. Chin Opt Lett 2016;14:022401.

[5] Xiang Y, Jiang X, You Q, Guo J, Dai X. Enhanced spin Hall effect of reflected light with guided-wave surface plasmon resonance. Photonics Res 2017;5:467–72.
[6] Weng S, Pei L, Wang J, Ning T, Li J. High sensitivity D-shaped hole fiber temperature sensor based on surface plasmon resonance with liquid filling. Photonics Res 2017;5:103–7.
[7] Weng S, Pei L, Wang J, Ning T, Li J. High sensitivity side-hole fiber magnetic field sensor based on surface plasmon resonance. Chin Opt Lett 2016;14:110603.
[8] Prasad PN. Plasmonics. In Nanophotonics. Hoboken, NJ, John Wiley & Sons, Inc., 2004, 129–51.
[9] Jia H, Yang F, Zhong Y, Liu H. Understanding localized surface plasmon resonance with propagative surface plasmon polaritons in optical nanogap antennas. Photonics Res 2016;4:293–305.
[10] Cuong NT, Tikhomirov VK, Chibotaru LF, et al. Experiment and theoretical modeling of the luminescence of silver nanoclusters dispersed in oxyfluoride glass. J Chem Phys 2012;136:174108.
[11] Tikhomirov VK, Vosch T, Fron E, et al. Luminescence of oxyfluoride glasses co-doped with Ag nanoclusters and Yb^{3+} ions. RSC Adv 2012;2:1496–501.
[12] Guo Z, Ye S, Liu T, Li S, Wang D. SmF_3 doping and heat treatment manipulated Ag species evaluation and efficient energy transfer from Ag nanoclusters to Sm^{3+} ions in oxyfluoride glass. J Non-Cryst Solids 2017;458:80–5.
[13] Kuznetsov AS, Cuong NT, Tikhomirov VK, et al. Effect of heat-treatment on luminescence and structure of Ag nanoclusters doped oxyfluoride glasses and implication for fiber drawing. Opt Mater 2012;34:616–21.
[14] Shestakov MV, Meledina M, Turner S, et al. The size and structure of Ag particles responsible for surface plasmon effects and luminescence in Ag homogeneously doped bulk glass. J Appl Phys 2013;114:073102.
[15] Lin H, Chen D, Yu Y, Zhang R, Wang Y. Molecular-like Ag clusters sensitized near-infrared down-conversion luminescence in oxyfluoride glasses for broadband spectral modification. Appl Phys Lett 2013;103:091902.
[16] Ueda J, Tanabe S, Ishida A. Surface plasmon excited infrared-to-visible upconversion in Er^{3+}-doped transparent glass ceramics. J Non-Cryst Solids 2009;355:1912–5.
[17] Zlatanovic S, Park JS, Moro S, et al. Mid-infrared wavelength conversion in silicon waveguides using ultracompact telecom-band-derived pump source. Nat Photonics 2010;4:561.
[18] Petersen CR, Møller U, Kubat I, et al. Mid-infrared supercontinuum covering the 1.4–13.3 μm molecular fingerprint region using ultra-high NA chalcogenide step-index fibre. Nat Photonics 2014;8:830–4.
[19] Kang S, Fang Z, Huang X, et al. Precisely controllable fabrication of Er^{3+}-doped glass ceramic fibers: novel mid-infrared fiber laser materials. J Mater Chem C 2017;5:4549–56.
[20] Chung WJ, Kim KH, Park BJ, Seo HS, Ahn JT, Choi YG. Radiative emission at mid-infrared wavelengths from rare-earth ions via nanocrystal formation in oxyfluoride glasses. J Am Ceram Soc 2010;93:2952–5.
[21] Tikhomirov VK, Driesen K, Görller-Walrand C, Mortier M. Mid-infrared emission in Yb^{3+}–Er^{3+}–Tm^{3+} co-doped oxyfluoride glass-ceramics. Mater Sci Eng 2008;146:66–8.
[22] Fedorov PP, Luginina AA, Popov AI. Transparent oxyfluoride glass ceramics. J Fluorine Chem 2015;172:22–50.
[23] Huang B, Zhou Y, Cheng P, Zhou Z, Li J, Yang G. The 1.85 μm spectroscopic properties of Er^{3+}/Tm^{3+} co-doped tellurite glasses containing silver nanoparticles. J Alloys Compd 2016;686:785–92.
[24] Ren J, Wagner T, Bartos M, et al. Intense near-infrared and midinfrared luminescence from the Dy^{3+}-doped $GeSe_2$–Ga_2Se_3–MI (M=K, Cs, Ag) chalcohalide glasses at 1.32, 1.73, and 2.67 μm. J Appl Phys 2011;109:033105.
[25] Tang J, Lu K, Zhang S, et al. Surface plasmon resonance-enhanced 2 μm emission of bismuth germanate glasses doped with Ho^{3+}/Tm^{3+} ions. Opt Mater 2016;54:160–4.
[26] Ma R, Zhao J, Chen X, et al. Stabilization of ultra-small $[Ag_2]^{2+}$ and $[Ag_m]^{n+}$ nano-clusters through negatively charged tetrahedrons in oxyfluoride glass networks: to largely enhance the luminescence quantum yields. Phys Chem Chem Phys 2017;19:22638–45.
[27] Wan J, Cheng J, Lu P. The coordination state of B and Al of borosilicate glass by IR spectra. J Wuhan Univ Technol Mater Sci Ed 2008;23:419–21.
[28] Kaur R, Singh S, Pandey OP. FTIR structural investigation of gamma irradiated $BaO–Na_2O–B_2O_3–SiO_2$ glasses. Phys B 2012;407:4765–9.
[29] Ebrahimi E, Rezvani M. Optical and structural investigation on sodium borosilicate glasses doped with Cr_2O_3. Spectrochim Acta Part A 2018;190:534–8.
[30] Dhara A, Mishra RK, Shukla R, et al. A comparative study on the structural aspects of sodium borosilicate glasses and barium borosilicate glasses: effect of Al_2O_3 addition. J Non-Cryst Solids 2016;447:283–9.
[31] Tian Y, Xu RR, Hu LL, Zhang JJ. Spectroscopic properties and energy transfer process in Er^{3+} doped ZrF_4-based fluoride glass for 2.7 μm laser materials. Opt Mater 2011;34:308–12.
[32] Stoica M, Patzig C, Bocker C, et al. Structural evolution of CaF_2 nanoparticles during the photoinduced crystallization of a $Na_2O–K_2O–CaO–CaF_2–Al_2O_3–ZnO–SiO_2$ glass. J Mater Sci 2017;52:13390–401.
[33] Avakyan LA, Heinz M, Skidanenko AV, et al. Insight on agglomerates of gold nanoparticles in glass based on surface plasmon resonance spectrum: study by multi-spheres T-matrix method. J Phys: Condens Matter 2018;30:045901.
[34] Zhang C, Ma J, Zhu D, et al. Tadpole-shaped Au nano-particles fabricated by laser fragmentation of Au nano-spheres in liquid. Chin Opt Lett 2016;14:081403.
[35] Nordlander P, Oubre C, Prodan E, Li K, Stockman MI. Plasmon hybridization in nanoparticle dimers. Nano Lett 2004;4:899–903.
[36] Tikhomirov VK, Méndez-Ramos J, Rodríguez VD, Furniss D, Seddon AB. Laser and gain parameters at 2.7 μm of Er^{3+}-doped oxyfluoride transparent glass–ceramics. Opt Mater 2006;28:1143–6.
[37] Judd BR. Optical absorption intensities of rare-earth ions. Phys Rev 1962;127:750–61.
[38] Ofelt GS. Intensities of crystal spectra of rare-earth ions. J Chem Phys 1962;37:511–20.
[39] Hubert S, Meichenin D, Zhou BW, Auzel F. Emission properties, oscillator strengths and laser parameters of Er^{3+} in $LiYF_4$ at 2.7 μm. J Lumin 1991;50:7–15.
[40] Jackson SD, King TA, Pollnau M. Modelling of high-power diode-pumped erbium 3 μm fibre lasers. J Mod Opt 2000;47:1987–94.
[41] Oermann MR, Ebendorff-Heidepriem H, Li Y, Foo T-C, Monro TM. Index matching between passive and active tellurite

glasses for use in microstructured fiber lasers: erbium doped lanthanum-tellurite glass. Opt Express 2009;17:15578–84.

[42] Wei T, Tian Y, Chen F, et al. Mid-infrared fluorescence, energy transfer process and rate equation analysis in Er^{3+} doped germanate glass. Sci Rep 2014;4:6060.

[43] Zhan H, Zhang A, He J, et al. Enhanced 2.7 μm emission of Er/Pr-codoped water-free fluorotellurite glasses. J Alloys Compd 2014;582:742–6.

[44] Sun X-Y, Jiang D-G, Sun Y-Z, et al. Eu^{3+}-activated B_2O_3–GeO_2–RE_2O_3 (RE=Y^{3+}, La^{3+} and Gd^{3+}) borogermanate scintillating glasses. J Non-Cryst Solids 2014;389:72–7.

[45] Li J, Zhang Z, Li X, et al. Luminescence properties and energy transfer of $YGa_{1.5}Al_{1.5}(BO_3)_4$:$Tb^{3+}$, Eu^{3+} as a multi-colour emitting phosphor for WLEDs. J Mater Chem C 2017;5:6294–9.

[46] Zhang WJ, Lin J, Cheng MZ, Zhang S, Jia YJ, Zhao JH. Radiative transition, local field enhancement and energy transfer microcosmic mechanism of tellurite glasses containing Er^{3+}, Yb^{3+} ions and Ag nanoparticles. J Quant Spectrosc Radiat Transfer 2015;159:39–52.

[47] Dexter DL. A theory of sensitized luminescence in solids. J Chem Phys 1953;21:836–50.

[48] McCumber DE. Theory of phonon terminated optical lasers. Phys Rev 1964;134:299–306.